ARL-TR-10104 • MAY 2025

High Strain Rate Experimental Characterization of Mode II Interlaminar Shear Response of UHMWPE Film Composites

by Frank D. Thomas, Subramani Sockalingam, Michael A. Sutton, C. Allan Gunnarsson, Tusit Weerasooriya, and Stephen L. Alexander

NOTICES

Disclaimers

The findings in this report are not to be construed as an official Department of the Army position unless so designated by other authorized documents.

Citation of manufacturer's or trade names does not constitute an official endorsement or approval of the use thereof.

Destroy this report when it is no longer needed. Do not return it to the originator.

ARL-TR-10104 ● MAY 2025

High Strain Rate Experimental Characterization of Mode II Interlaminar Shear Response of UHMWPE Film Composites

Frank D. Thomas, Subramani Sockalingam, and Michael A. Sutton
University of South Carolina

C. Allan Gunnarsson and Tusit Weerasooriya
DEVCOM Army Research Laboratory

Stephen L. Alexander
SURVICE Engineering Company

REPORT DOCUMENTATION PAGE

1. REPORT DATE	2. REPORT TYPE	3. DATES COVERED	
		START DATE	END DATE
May 2025	Technical Report	1 October 2023	31 March 2025

4. TITLE AND SUBTITLE
High Strain Rate Experimental Characterization of Mode II Interlaminar Shear Response of UHMWPE Film Composites

5a. CONTRACT NUMBER	5b. GRANT NUMBER	5c. PROGRAM ELEMENT NUMBER
W911NF2020231, W15P7T19D0126		
5d. PROJECT NUMBER	**5e. TASK NUMBER**	**5f. WORK UNIT NUMBER**

6. AUTHOR(S)
Frank D. Thomas, Subramani Sockalingam, Michael A. Sutton, C. Allan Gunnarsson, Tusit Weerasooriya, and Stephen L. Alexander

7. PERFORMING ORGANIZATION NAME(S) AND ADDRESS(ES)	8. PERFORMING ORGANIZATION REPORT NUMBER
DEVCOM Army Research Laboratory ATTN: FCDD-RLA-TB Aberdeen Proving Ground, MD 21005	ARL-TR-10104

9. SPONSORING/MONITORING AGENCY NAME(S) AND ADDRESS(ES)	10. SPONSOR/MONITOR'S ACRONYM(S)	11. SPONSOR/MONITOR'S REPORT NUMBER(S)

12. DISTRIBUTION/AVAILABILITY STATEMENT
DISTRIBUTION STATEMENT A. Approved for public release: distribution unlimited.

13. SUPPLEMENTARY NOTES
ORCIDs: Frank Thomas, 0000-0001-5622-3412; Subramani Sockalingam, 0000-0003-4335-2009; Michael A. Sutton, 0000-0002-6946-5047; Tusit Weerasooriya, 0000-0003-3299-2166; C. Allan Gunnarsson, 0000-0002-8472-5193

14. ABSTRACT
To accurately model delamination behavior in ballistic impact simulations of laminated composite materials, interfacial traction–separation parameters must be experimentally determined. For material systems such as ultra-high-molecular-weight polyethylene (UHMWPE) films, which exhibit a high degree of strain-rate dependency in their mechanical response, high strain rate (HSR) characterization methodologies are needed for obtaining material deformation and failure behavior as a function of loading rate, especially to obtain the delamination response. This report discusses a new method using a tensile split-Hopkinson pressure bar to induce simple shear in a pre-cracked specimen for the purpose of extracting Mode II traction–separation parameters. Experiments are performed on UHMWPE Tensylon composites, and digital image correlation is used to extract full-field displacement and strain data for analysis. In this study, local shear strain rates on the order of 10^4 s^{-1} are reached in the specimen, and results are compared to equivalent quasi-static values. Linear increases in shear strength and apparent interfacial stiffness are observed, and the energy release rate appears to vary quadratically with strain rate. This study provides a methodology for obtaining HSR Mode II shear fracture response in laminated composites.

15. SUBJECT TERMS
ultra-high-molecular-weight polyethylene, UHMWPE, Tensylon, films, traction–separation, Mode 2, GIIC, interlaminar shear, shear failure, digital image correlation, DIC, Sciences of Extreme Materials, Terminal Effects

16. SECURITY CLASSIFICATION OF:			17. LIMITATION OF ABSTRACT	18. NUMBER OF PAGES
a. REPORT	b. ABSTRACT	C. THIS PAGE		
UNCLASSIFIED	UNCLASSIFIED	UNCLASSIFIED	UU	47

19a. NAME OF RESPONSIBLE PERSON	19b. PHONE NUMBER *(Include area code)*
Tusit Weerasooriya	(520) 691-6332

STANDARD FORM 298 (REV. 5/2020)
Prescribed by ANSI Std. Z39.18

Contents

List of Figures

List of Tables

1. Introduction

When modeling the ballistic performance of a composite structure, many material parameters such as stiffness and strength must be determined for accurate predictive capabilities. Figure 1 presents a simplified diagram of a ballistic impact on a laminated composite structure, highlighting various features of the deformation response. One characteristic that is essential to characterizing the damage and energy dissipation response is the interlaminar behavior, especially the Mode II interlaminar shear (ILS) response caused by relative sliding between plies.[1] The sliding is driven by opposing tension and compression between orthogonal plies arising from anisotropic Poisson expansion.[2] Quantifying the associated properties (e.g., interfacial stiffness [E_T], strength [τ_{max}], and critical energy release rate or fracture toughness [G_{IIC}]) in a controlled experiment is typically conducted at quasi-static (QS) rates with established methods such as end-notched flexure (ENF), but these methods depend on the material distant from the crack tip deforming elastically. Ultra-high-molecular-weight polyethylene (UHMWPE) cross-ply unidirectional (UD) composites feature a combination of low weight, high stiffness and strength in the reinforcement direction and low ILS strength properties.[3,4] Low ILS strength in a UHMWPE [0°/90°] cross-ply reinforcement architecture induces significant ILS deformation during impact resulting in large out-of-plane deformation, which reduces the pressure exerted by the projectile.[3,5,6] Under bending loads, materials with low ILS strength are likely to undergo inelastic deformation in areas distant from the crack tip, which causes standard analytical equations to no longer represent the stress state and overestimate G_{IIC}. Furthermore, even materials that are well-suited for ENF loading at QS rates demonstrate similar problems (e.g., crack initiation distant from the crack tip) at high strain rates (HSRs), which are equivalent to the time scales over which damage by ballistic impact occurs. Therefore, a consistent and reliable method for HSR characterization of ILS behavior needs to be developed, especially for composite materials with low shear strength.

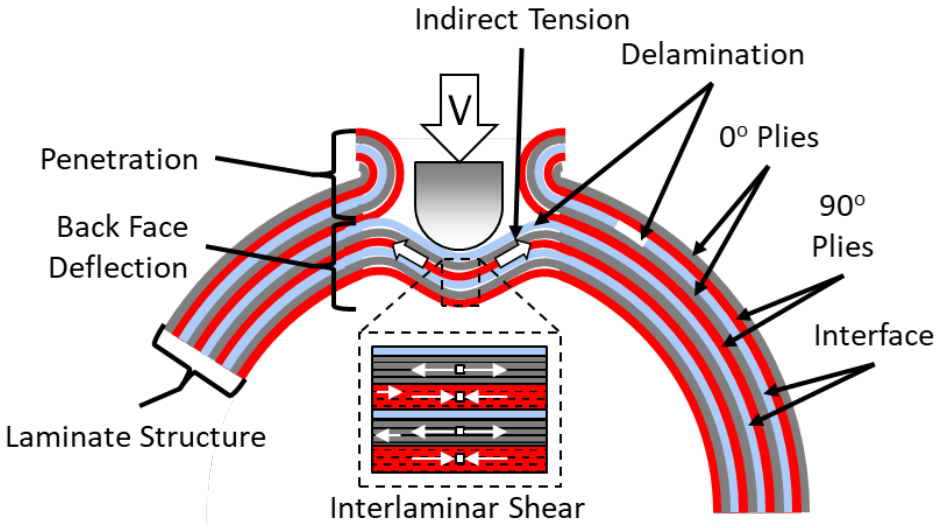

Figure 1. Ballistic impact diagram.

In this report, a novel experimental methodology incorporating new specimen and fixture designs is presented for obtaining Mode II ILS parameters in film-based composite materials at high shear rates (>1000 s^{-1}), and preliminary results are presented. Finally, applications, challenges, and future developments to improve accuracy are discussed.

2. Methods

2.1 Materials

UHMWPE Tensylon is a film-based composite material, where individual UD layers are melt-drawn from bulk material to produce planar sheets with highly oriented crystallinity, resulting in high stiffness and strength in the axial (0°) direction and low strength in the orthogonal (90°) direction. As a result, material is commercially available as a sheet comprising two bonded UD layers oriented orthogonally to each other (0°/90°), and consolidated laminates are typically produced with a cross-ply ($[0°/90°]_n$) architecture. Studies were performed to quantify the tensile properties of single UD layers[7] as a function of strain rate and orthotropic properties of consolidated laminates,[8] but only preliminary work on the more complex interlaminar failure has been performed.[2,9,10]

To promote consolidation, one side of the sheet is coated with a thermoplastic that is melted to fuse sheets together, forming the final composite laminate. Unlike typical (fiber-based) composites, the material between the individual UD film layers is the only true matrix material in a film-based composite,[11] and in the final

consolidated state it is largely responsible for the interfacial properties including those governing the Mode II interlaminar fracture behavior.

2.2 Specimen Design and Fabrication

Schematics of the specimen architecture used in experiments are shown in Figure 2. Because UHMWPE-based composite materials presented difficulties in obtaining a pure Mode II response via typical methods (e.g., ENF at QS rates, the failure of which also may be dominated by the significant Mode I component), specimens are designed to induce failure under a simple shear-type load. Furthermore, a pre-crack has been added to induce crack growth and subsequent failure at a specific location with a predetermined defect, making energy release rate analysis more feasible.

Two specimen sizes were chosen based on previous fracture characterization methods: a thin specimen similar to rigid double cantilever beam specimens,[12] consisting of 4 UD layers or 2 as-delivered sheets to minimize structural effects during loading, and a thick specimen similar in dimensions to the center section of an Arcan butterfly specimen previously studied,[13,14] consisting of 120 UD layers or 60 as-delivered sheets to allow for measurement of full-field strain and displacements localized at the crack tip via digital image correlation (DIC) using Correlated Solutions' VIC-2D software. In reference to the coordinate system shown in Figure 2, for all specimens, length (x-direction) is nominally 38.1 mm, width (z-direction) is 6.4 mm, and pre-crack length is 19.05 mm. The specimen height (y-direction, ply stacking direction) was nominally 0.22 and 6.6 mm for thin and thick specimens, respectively. For both sizes, specimens were produced with two different stacking sequences, one with a standard cross-ply lay-up (0°/90°), and one that is symmetrical about the crack plane interface (0°/0°) with the intent of characterizing the interfacial material and excluding adjacent ply failure as a compounding means of crack propagation from the initial notch. Specimen designations shown in figures in Sections 3.1–6 contain either a "C" to denote a specimen with a cross-ply configuration at the crack plane or a "U" to denote a unidirectional configuration at the crack plane. As the material is only commercially available as a cross-ply stack, each specimen type does contain alternating 0° and 90° layers; only the ply orientations at the crack plane are controlled to produce the desired local structure at the crack plane.

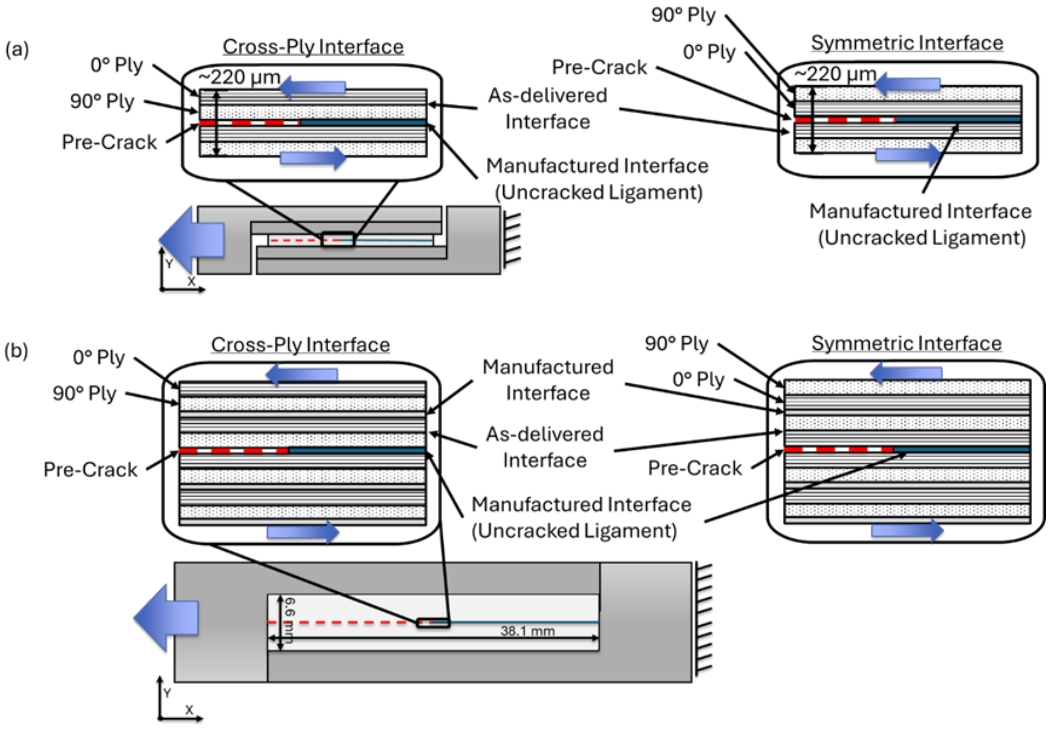

Figure 2. Standard lay-up architecture for (a) thin and (b) thick specimens. Blue gradient-shaded arrows indicate loading. Specimen length (x-direction) and height (y-direction) are indicated in (b) for thick specimens, while the width (z-direction, out-of-plane) was 6.4 mm. Thin specimens had the same length and width, but a height of only 0.22 mm.

Thick specimen fabrication details are illustrated in Figure 3. Thick specimens are laid up in a rectangular mold that was custom designed and fabricated to limit ply squeeze-out and ensure even pressure distribution with the significantly higher number of sheets. A 0.001-inch-thick copolymer or fluoropolymer mold release film is applied on the top and bottom of the ply stack to prevent adhesion to the mold or press plate surface. Along each edge at the midplane of the ply stack, a strip of 0.0005-inch-thick fluorinated ethylene propylene (FEP) film is laid to create the pre-crack. Thin specimens are constructed and processed identically, with the exception being that the ply stacks with FEP film inserts are laid directly on the press plates with no mold because the risk of squeeze-out is small compared to the thick specimens, and double-sided tape applied at a few noncritical points is sufficient to keep the sheets aligned relative to each other before and during consolidation. The ply stacks are consolidated under conditions previously reported in literature, nominal pressures of 20.7 MPa and temperatures of 110 °C,[3] and specimens are extracted from the edges with the pre-crack. Thin specimens, which do not require a mold for consolidation, can be cut out with razor blades, but waterjet cutting is necessary to extract thick specimens. After extraction, the thick specimens are also wet sanded to remove any resulting taper, ensuring consistent uniform dimensions through the thickness.

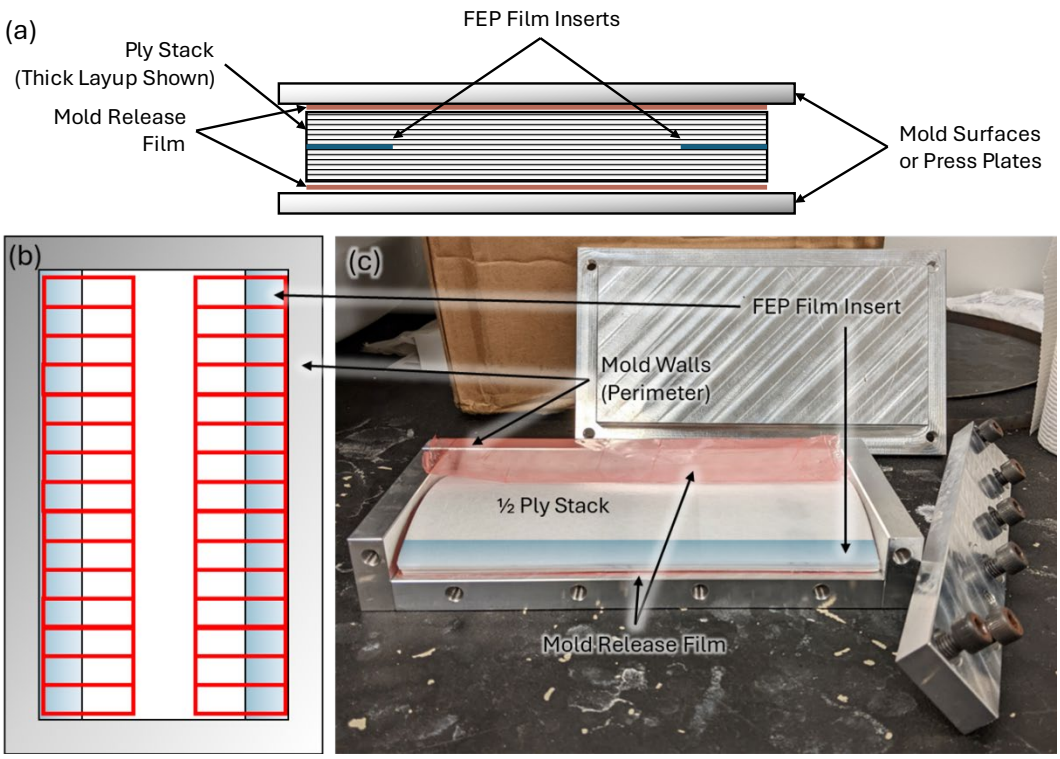

Figure 3. Specimen lay-up and extraction details. (a) Stacking diagram showing through-thickness positioning of the mold release film and FEP inserts relative to the ply stack and mold surfaces. (b) Diagram showing specimen extraction from top view of a typical specimen panel inside the mold (walls represented by gray-to-white gradient). Red rectangles represent individual specimens, and shaded left and right edges show the FEP film positioning. Because these film inserts form the pre-crack, the interior edges (vertical lines passing through the red rectangles) represent the crack tip position through each specimen. (c) Photo of partially disassembled mold with in-progress lay-up highlighting FEP film insert (blue) and mold release film (red). Release film is oversized relative to the panel, so some excess can be seen coming out on top of the stacked plies.

Experimental fixtures, shown in Figure 4, are pairs of substrates (specimen holders) designed to rigidly support the specimens in the through-thickness direction and induce simple shear in the loading direction. The large threads on the end are intended to thread into the tensile SHPB as well as adapters (shown in Figure 5) for use in uniaxial testing machines at QS rates. The M3-sized holes in the upper substrate are close-fit clearance holes to allow free rotation of the screws with some lateral constraint, but the M3 holes are tapped in the lower substrate to be able to introduce the clamping force without the need for additional nuts. Specimens are joined to the fixtures by adhesive bonding, so an extensive preliminary investigation was performed to identify a suitable method of bonding the UHMWPE specimens to the fixtures to ensure that deformation was localized within the specimen rather than at the specimen–fixture bond. Preliminary experiments found that Loctite 426 toughened cyanoacrylate adhesive bonds well with a relatively short (~30–60 min) cure time. For this and other adhesives (e.g.,

epoxy or acrylic), corona plasma treatment is necessary for all specimens to form sufficiently strong-enough bonds with the fixtures because of the low surface free energy, which is typical of UHMWPE and similar polymers. Transverse screws (Figure 4) apply even pressure across the bonding surfaces of the specimens and prevent damage to the specimen when loading into the tensile split-Hopkinson pressure bar (SHPB). Thick specimens have speckles for DIC applied directly via spray paint, and the thin specimen fixtures have flat regions where speckles are applied, though the specimen itself has a height that is too small (only 0.22 mm [see Figure 2a]) to reliably speckle and image, using ultra-high-speed (UHS) imaging. Once adhesive bonding is complete, the threaded fixture-bonded specimen assembly is threaded into the SHPB, an initial image is taken, and the transverse screws are removed.

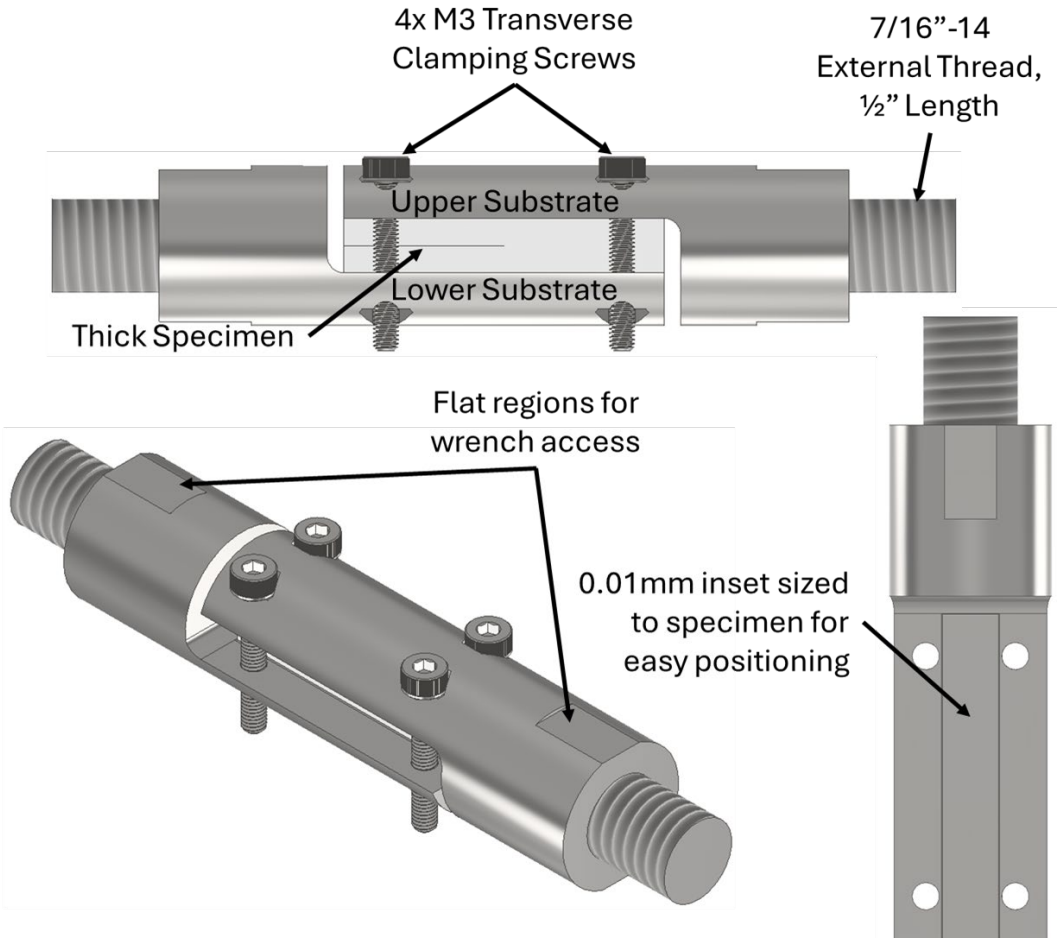

Figure 4. Simple shear fixture for thick specimens. The thin specimen fixture is identical, aside from the specimen mounting surface being raised to account for the reduced specimen thickness and to provide a flat surface for DIC speckle application.

2.3 Preliminary Quasi-Static Experiments

The specimen design introduced in Section 2.2 was developed with HSR characterization in mind, but QS characterization has also been performed with the same fixture to verify feasibility and provide baseline data. Figure 5 presents the fixture–specimen assembly with QS adapters both inside and outside the uniaxial testing machine. Visible screws joining the fixtures are removed before running the experiment and are used to promote adhesive curing and protect the specimen while loading the assembly into the experimental apparatus. This is consistent with the procedure in the HSR experiments.

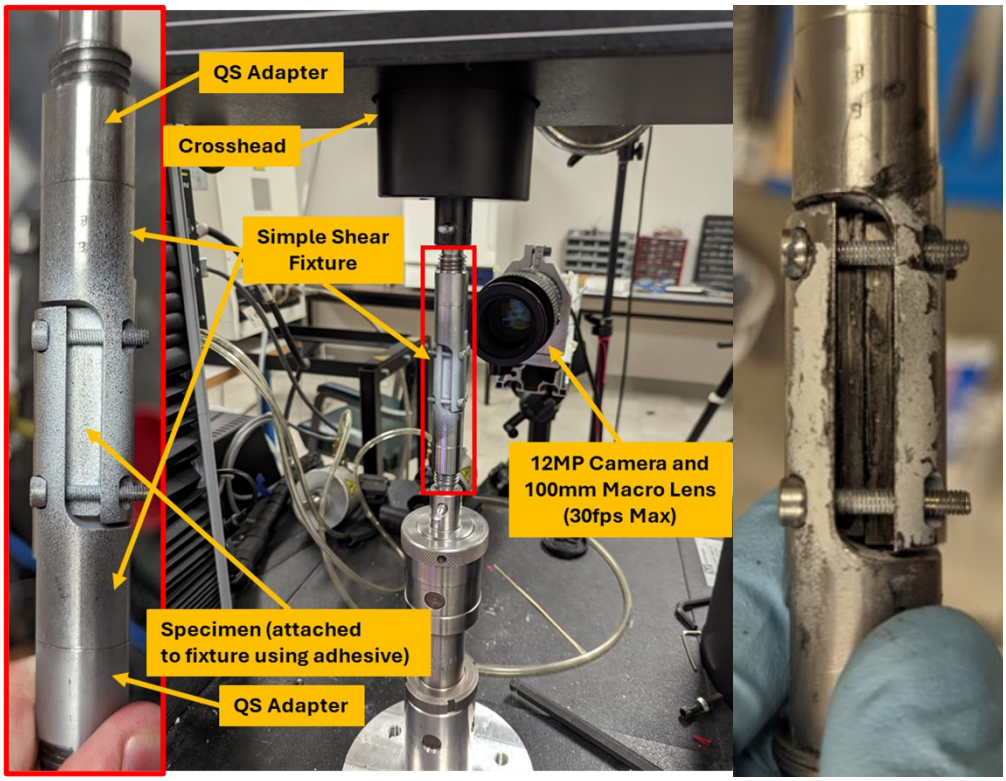

Figure 5. QS experimental setup. The left image is a close-up of a speckled thick specimen in the simple shear fixture with adapters for use in the uniaxial testing machine. The center image depicts the in situ configuration. The right image depicts a thin specimen mounted in a modified simple shear fixture prior to speckling. The transverse clamping screws assist with safe specimen loading and are removed prior to running the experiment.

Data reduction to obtain Mode II traction–separation responses from measured traces are discussed further in Section 2.5, but experimental QS traction–separation data from a single representative specimen is presented in Figure 6. As the focus of this report is on the HSR characterization, this single experiment is used with comparisons to the HSR data rather than aggregate data across multiple experiments. Shear tractions are based on average shear stress, crosshead load divided by interfacial area (the specimen width multiplied by the uncracked

ligament length), and separations are based on tangential displacement near the crack tip as determined by DIC measurements. Based on these definitions, the traction–separation data takes the form of an initial linear region with an apparent interfacial stiffness of 502.5 MPa/mm, which transitions to a plateau region as the peak load is reached and corresponds to an average stress of 3.41 MPa. Shortly after reaching this point, unstable crack growth occurs resulting in a sharp drop in load. Assuming the area under this curve to be equivalent to a J-integral approximation of the Mode II critical energy release rate (G_{IIC}), G_{IIC} is equal to 65.5 J/m^2.

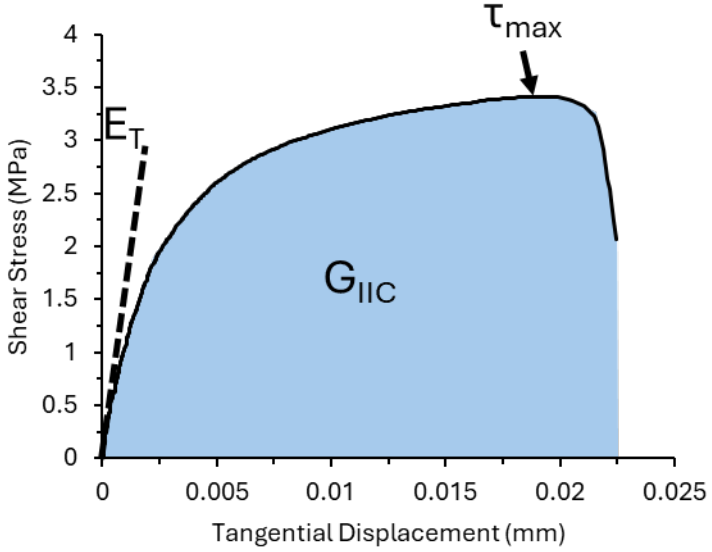

Figure 6. Representative QS apparent traction–separation curve.

2.4 HSR Experiments

Experimental apparatus schematics for thin and thick specimens are shown in Figures 7 and 8, respectively, and Figure 9 shows a photograph of the setup with a thick specimen loaded. Specimens are loaded in tension by a strain pulse produced by launching a striker at the incident bar flange at nominal pressure settings of 20 and 60 psi, which result in experimental groups corresponding to a lower and higher dynamic loading rate. (Due to the complexity associated with this loading, defining and quantifying each of these rates are discussed at length later in this report.) On both the incident and transmission bars (3/4-inch-diameter C300 maraging steel, 9-ft-long incident bar, 6-ft-long transmission bar, and 18-inch striker), conventional strain gages are placed to measure the incident, transmitted, and reflected strain signals in the bar, which are typically used to infer strain rate and stress in the specimen. However, due to the relatively low interfacial properties, transmitted loads are also measured by a high-sensitivity semiconductor strain gage to measure loading in the specimen. Semiconductor strain gages are known to be highly dependent on environmental conditions; therefore, periodic gage calibrations were

performed. Furthermore, as the loading is simple shear rather than axial tension, and the fixture geometry is nonstandard relative to a typical tension SHPB grip, shear strain rates are assessed based on DIC data rather than the reflected and transmitted strain signal as is typical in SHPB data analysis with dynamic equilibrium assumption.

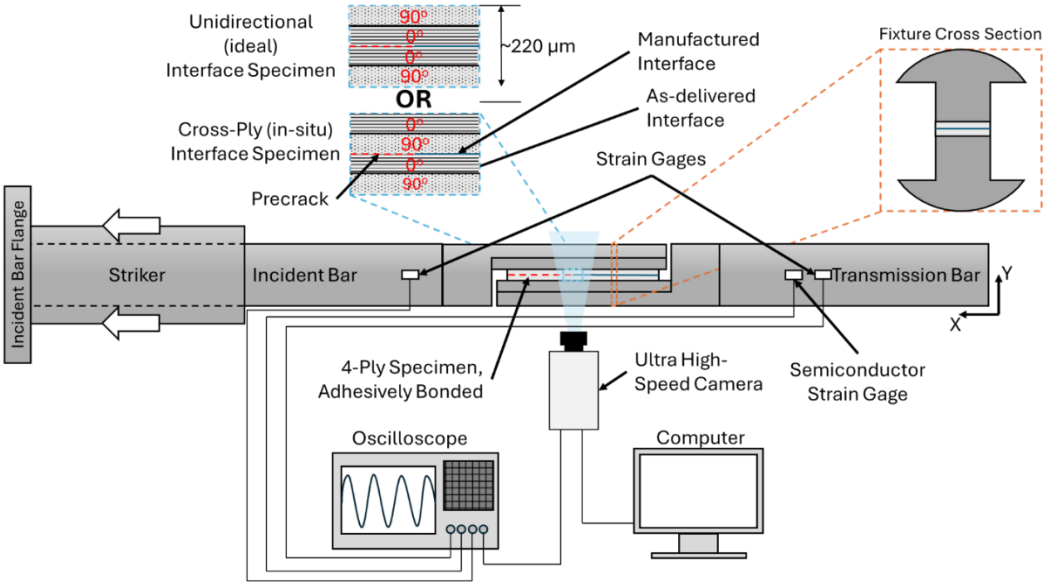

Figure 7. Thin specimen experiment schematic. Flat sides of the fixture are speckled and recorded by a UHS camera to measure rigid body motion from DIC to estimate shear displacements and strain rates in the thin specimen. Pre-crack is oriented toward the source of load introduction (incident bar).

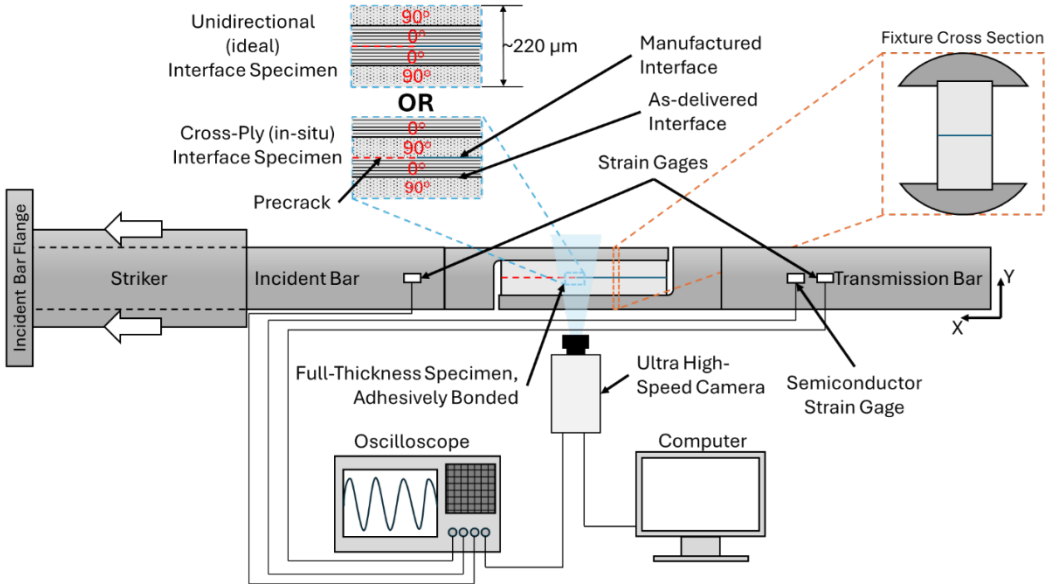

Figure 8. Thick specimen experiment schematic. Specimen sides are speckled and recorded by a UHS camera for full-field deformation measurement via DIC to directly measure tangential separations, shear strains, and strain rates. Pre-crack is oriented toward the source of load introduction. The inset for specimen seating shown in the fixture cross section is exaggerated for illustrative purposes.

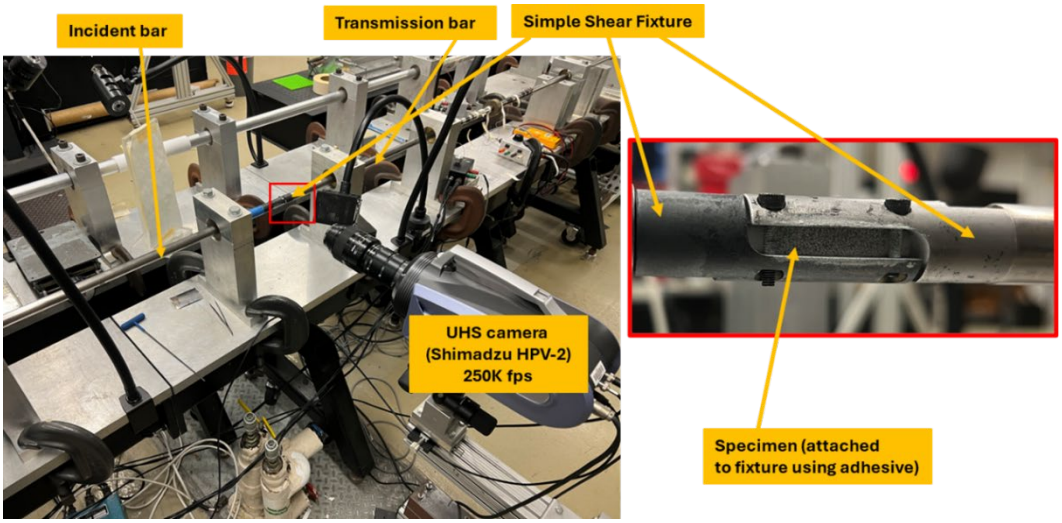

Figure 9. HSR experimental setup. The tensile SHPB is loaded with a thick specimen and the transverse clamping screws are still in place. They are removed after taking an initial reference image before the experiment is performed.

Specimen deformation during loading is captured by a UHS Shimadzu HPV-2 camera at 250,000 fps and 312 × 260 resolution using a halogen lamp to illuminate the specimen. To limit unwanted heating in the specimen or optical equipment, the lamp is powered on just before taking a static image or launching the striker and powered off immediately after static imaging or running an experiment. The camera outputs a continuous square wave signal to another channel to identify time points

for each captured image (every 4 μs here for 250,000 fps), and upon receiving a trigger signal from the incident strain gage, it captures 102 sequential images at which point image capture and the corresponding signal cease. Thus, images can easily be synchronized with the incident strain pulse by applying a 404-μs time offset from the time of the final frame.

Before each experiment, a consistent setup procedure is followed. The fixture is loaded into the bar, a static image is taken as reference, transverse screws are removed, another static image is taken, the strain gages are balanced, and the camera is set to be triggered by the incident strain gage. After setup is complete, the striker is launched at 20- or 60-psi tank pressure (corresponding velocities were calculated and are reported in Section 3.4) with a single layer of copper tape as a wave shaper for the 60-psi experiments only, and data is recorded for reduction and analysis.

2.5 Data Reduction

Semiconductor strain gage data (ε_{sc}) is used in conjunction with the transmission bar properties (area A_B and modulus E_B) to calculate specimen load P according to Equation 1. Average stress σ_{avg} is calculated by dividing P by the interfacial area A_{int} (Equation 2). This assumes stress concentrations at the crack tip are negligible. Conventional strain gage data in the incident (ε_I), reflected (ε_R), and transmitted (ε_T) pulses, and wave speed in the bar material (C_B) are used to obtain gross relative displacements du_{bar} based on the motion of the incident bar relative to the transmission bar according to Equation 3. This gross displacement measurement is primarily used for comparison with the more precise local displacements from DIC measurements.

$$P = A_B E_B \varepsilon_{sc} \tag{1}$$

$$\sigma_{avg} = \frac{P}{A_{int}} \tag{2}$$

$$du_{bar} = C_B \int_0^t (\varepsilon_I - \varepsilon_R - \varepsilon_T) dt \tag{3}$$

Calibration and experiment progression images are loaded in VIC-2D DIC software for displacement and strain analysis. For thin specimens, rectangular areas of interest (AOIs) are drawn over the top and bottom rigid substrates, as the specimen itself is typically not speckled and not large enough to effectively image at high rates. Figure 10 provides an example of a thin specimen with these two rectangular AOIs, denoted as 1 and 2, drawn over the bottom and top substrates, respectively. For measuring displacements along the crack plane and far-field strains in the thick

specimens, two rectangular AOIs were drawn as shown in the example in Figure 11. One rectangular AOI was drawn on the UHMWPE specimen in the region below the crack plane (denoted as 1 in Figure 11) and the other AOI was on the specimen in the region above the crack plane (denoted as 2). This limits the effects of bias from exceptionally small subset and step sizes as further explained in the Appendix, which also provides additional details regarding the methodology used for DIC analysis.

DIC analysis of static imaging is used to inform DIC parameter selection and assess the noise floor in displacements and strains. Final DIC parameters are listed in Table 1. Noise floor values are equivalent to the standard deviation of the displacement or strain data under static imaging. The reference speckle image is from the specimen prior to screw removal, so some minor deformation is often observed prior to high-rate loading, but specimens with local interfacial displacement outside the typical range are excluded because significant damage and initial crack growth has likely occurred prior to the experiment. For thin specimens, average substrate displacements (u_{sub1}, u_{sub2}) are extracted from regions 1 (fixed) and 2 (moving) as seen in Figure 10. For quantities that are expected to be consistent over a large region (e.g., thin specimen rigid substrate displacement and thick specimen far-field strains), the "Inspect Rectangle" or "Inspect Polygon" feature is used to average the data over a large area such as an entire AOI. For thick specimens, displacements at the crack tip x position (u_{local1}, u_{local2}) are extracted from regions 1 (fixed) and 2 (moving) as seen in Figure 11. Finally, thick specimen shear strains in each AOI (γ_{DIC}, outside the crack plane and relatively distant from the crack tip) are also calculated by VIC-2D and are examined primarily for the purpose of obtaining an approximate value for the elastic shear modulus.

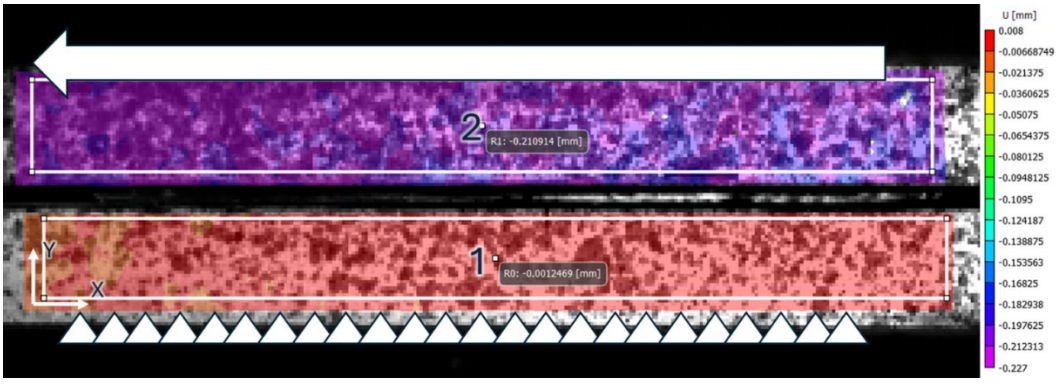

Figure 10. DIC average displacement data extraction for thin specimens. Regions 1 and 2 noted on the figure (bounded by white rectangles) are the sources for average displacements u_{sub1} and u_{sub2}, respectively.

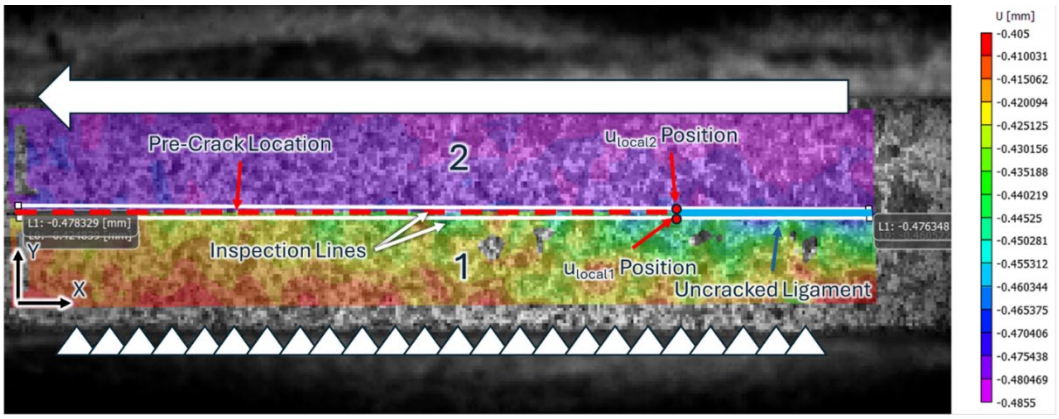

Figure 11. DIC local displacement data extraction for thick specimens. Pre-crack and uncracked ligaments are noted by red dashed and blue solid lines, respectively. Displacements are sampled along each white line, separated by 0.1 mm, straddling the extended crack front, approximately equal distance from it on either side, and tangential separations can be obtained from pointwise differences along the length. Displacements u_{local1} and u_{local2}, just ahead of the crack tip (marked with red dots), are used for local tangential separation in thick specimens. U represents the displacement in the horizontal or pre-crack front direction.

Table 1. DIC parameters.

Parameter	Value	Notes
Approximate magnification	0.08 mm/pixel	. . .
Subset size	13 × 13 pixels^2	~1 × 1 mm^2
Step size	1 pixel	~0.08 mm
Strain filter size	5 data points	0.4 mm strain window diameter
Displacement noise floor (U)	6.76*10^{-4} mm	0.00831 pixels
Full-field shear strain noise floor (γ_{DIC})	0.226%	Double the Lagrange tensorial shear strain

Tangential separation (du), used in the approximate traction–separation relation, is taken to be u_{sub2}-u_{sub1} for thin specimens and u_{local2}-u_{local1} for thick specimens. Therefore, the tangential separation calculated for thin specimens is referred to as an "average" value, du_{avg}, whereas the tangential separation calculated for thick specimens is referred to as a "local" value, du_{local}:

$$du_{avg} = u_{sub2}\text{-}u_{sub1} \tag{4}$$

$$du_{local} = u_{local2}\text{-}u_{local1} \tag{5}$$

Substrate or crack tip relative velocity (V_{ct}) is evaluated according to Equation 6, where du is either du_{avg} or du_{local}, depending on the specimen type:

$$V_{ct} = \frac{d(du)}{dt} \tag{6}$$

Because the deformation is primarily simple shear, and displacement normal to the loading direction (dv) should be negligible, crack tip shear strain (γ_{xy}) is

approximated according to Equation 7. The vertical distance (*dy*) over which shear strain is evaluated is assumed to be the gap between the substrates (nominally, 0.22 mm) in the case of thin specimens and directly calculated in the case of thick specimens (typically, 0.1 mm). The instantaneous shear rate ($\dot{\gamma}_{xy}$) is approximated according to Equation 8.

$$\gamma_{xy} = \frac{dv}{dx} + \frac{du}{dy} \approx \frac{du}{dy} \tag{7}$$

$$\dot{\gamma}_{xy} = \frac{d\gamma_{xy}}{dt} = \frac{d}{dt}\left(\frac{du}{dy}\right) = \frac{1}{dy}\frac{d(du)}{dt} = \frac{V_{ct}}{dy} \tag{8}$$

Because V_{ct} is evaluated between the substrates for thin specimens and on the material near the crack tip for thick specimens, both V_{ct} and $\dot{\gamma}_{xy}$ will vary somewhat between specimen types at similar loading rates. V_{ct} is expected to be larger for thin specimens, but $\dot{\gamma}_{xy}$ will be smaller due to an increase in *dy*. Thin specimen values are useful as confirmation of a general shear strain rate range, but thick specimen values take priority in terms of material parameter identification because they are more directly indicative of the material response.

3. Results

For each specimen type (thin and thick) at each rate (low and high), seven to nine successful experiments were performed in which no adhesive failure at the upper and lower specimen surfaces is observed and interfacial failure is induced along the pre-crack plane. Differences between cross-ply and UD interface responses are negligible, so they are averaged together to improve the sample sizes. Table 2 provides an overview of the average parameters calculated from the experiments performed on Tensylon composites. Additional information for each of the parameters is provided below.

Table 2. Experimentally measured apparent traction–separation parameters for Tensylon composite panels. Experiments referred to as having lower and higher rates are both loaded dynamically via Hopkinson bar, as opposed to the QS data, which was obtained via universal testing machine.

Experimental group	Average substrate/ crack tip relative velocity, V_{ct} (m/s)	Average shear strain rate, $\dot{\gamma}_{xy}$ (s^{-1})	Shear strength, τ_{max} (MPa)	Apparent interfacial stiffness during loading, E_T (MPa/mm)	GIIC (J/m^2)	Through-thickness shear modulus, G_{12} (GPa)
Thin, lower strain rate (n = 7)	3.71 ±0.75	1.68e4 ±3.4e3	7.26 ±3.09	887.4 ±561.4	1018 ±506	NA
Thin, higher strain rate (n = 7)	8.81 ±0.56	4.01e4 ±2.5e3	15.0 7±4.48	1004.7 ±382.9	3997 ±1063	NA
Thick, lower strain rate (n = 8)	2.78 ±1.81	2.55e4 ±1.79e4	7.86 ±1.83	845.9 ±448.9	671 ±266	2.701 ±1.446
Thick, higher strain rate (n = 9)	5.71 ±1.78	5.76e4 ±1.74e4	14.07 ±2.62	1458.3 ±619.6	3846 ±1527	4.123 ±2.164
Combined, lower strain rate (n = 15)	NA	NA	7.58 ±2.42	865.3 ±486.1	833 ±421	NA
Combined, higher strain rate (n = 16)	NA	NA	14.50 ±3.46	1259.8 ±563.4	3912 ±1305	NA
Thick, QS strain rate (n = 1)	1.1856e-5	0.0597	3.41	502.5	65.5	0.309

3.1 Bar-Level Loading and Displacement

Representative strain gage signals are presented in Figure 12. Thick specimen experiments are presented and discussed, and typical strain gage data from thin specimens are similar. At both nominal loading rates, the incident pulse shape has only minor oscillations at the initial peak, though a single layer of copper tape is used as a pulse shaper for the high-speed experiments. Reflected pulses are of similar magnitude to the incident pulse, but the shape of the pulse is not consistent with incident. This is likely due to the fixture inertia rather than representative of the load state in the specimen because of the much smaller transmitted signal amplitude. Transmitted pulses are quite small but nonnegligible, as can be seen in the isolated transmitted signals. Although the conventional gage requires a

minimum 21-point moving average filter (4-μs window size) to make features identifiable, time series data closely resembles the unfiltered semiconductor strain gage data, confirming that calibration is consistent even at very low amplitudes. The differences in position between the two gages are visible as a minor time offset, and all data is ultimately time shifted based on distance between gage and bar end to properly synchronize the final traction, separation, and strain data.

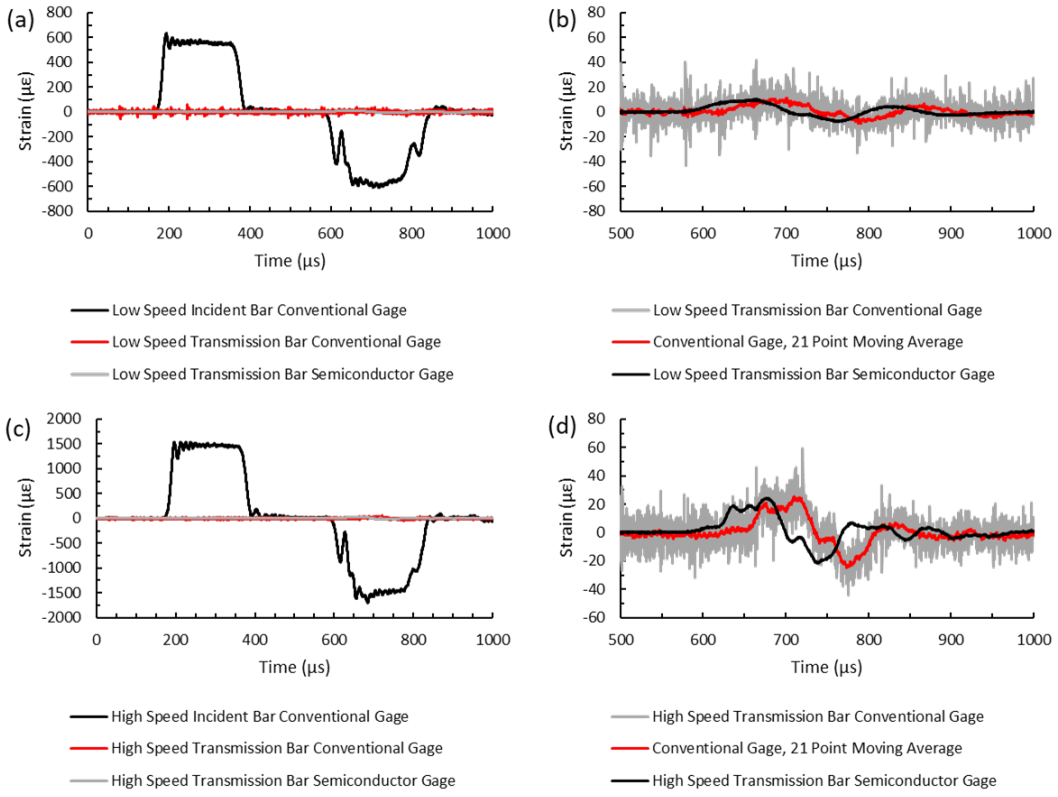

Figure 12. Representative raw strain gage output data for thick specimens at low and high speeds. Transmitted pulses are isolated to visualize the data because of the large differences in scale between incident and transmission bar gage signals. Slight temporal offsets between the conventional and semiconductor gages are expected because they are placed at different points along the transmission bar.

Transmitted force data (calculated from Equation 1 using semiconductor strain gage data and transmission bar properties with an 11-point moving average filter applied for mild smoothing) is plotted as a function of time in Figure 13. Figure 13a and b present data for thin specimens at lower and higher rates, respectively, and Figure 13c and d present data for thick specimens at lower and higher rates. Independent of specimen design, increases in strain rate correlate with increases in peak load, in spite of some overlap due to a wide spread in peak load as well as some variation in uncracked ligament length from specimen to specimen. Thin specimens also typically had a smaller width on average, which explains the difference in force axes used for thin specimens compared to that of the thick

specimens. It is shown in the following sections that differences between specimens for a given nominal loading rate are much smaller once specimen bonded area (uncracked ligament multiplied by specimen width) is taken to obtain the average shear stress. Cross-ply and UD interface specimens, which are denoted by "C" and "U" in specimen designations, respectively, are combined in each experimental group, as the responses are statistically indistinguishable.

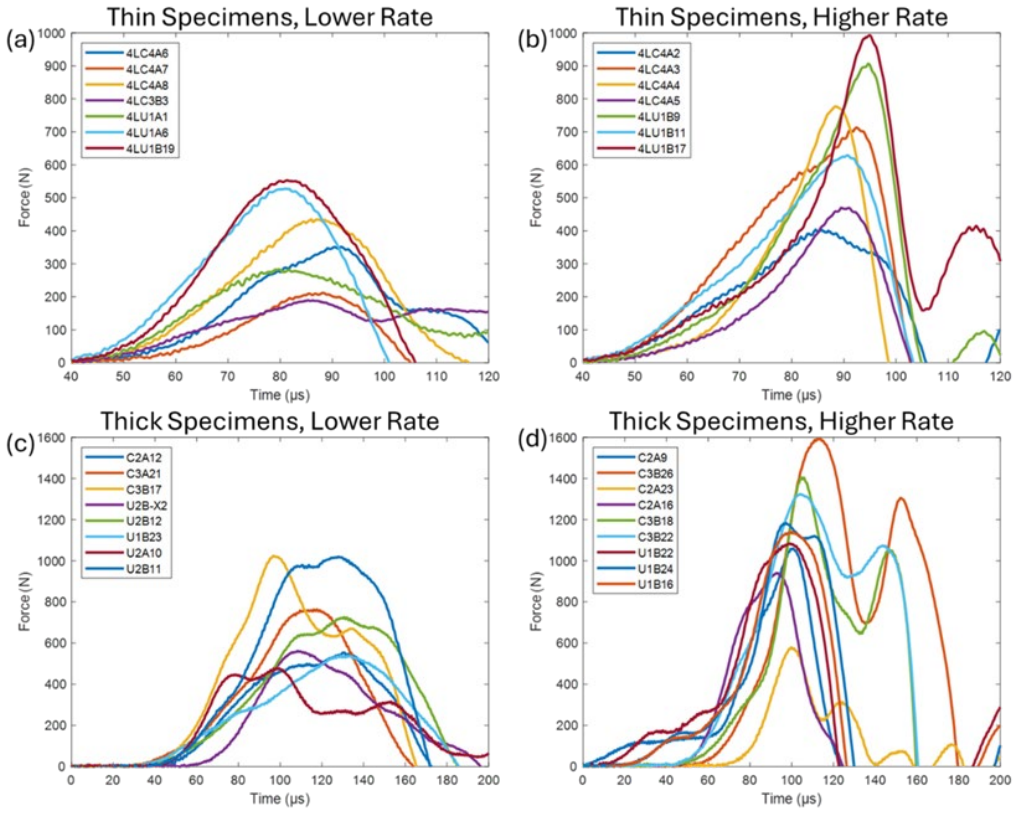

Figure 13. Raw load-time data for (a) thin specimens at the lower rate, (b) thin specimens at the higher rate, (c) thick specimens at the lower rate, and (d) thick specimens at the higher rate. Data is derived from semiconductor strain gage signals. Axes are consistent for each specimen type at varying rates, but differences in specimen architecture and response necessitated varying scales to best highlight the gross loading response over time.

Representative bar relative displacement data (du_{bar}) is compared with DIC-based tangential separation data in Figure 14 for thin (du_{avg}) and thick specimens (du_{local}) at the higher rate (lower rate data is similar but scaled down compared to high rate). Gross bar displacement data is essentially the same for both, but some minor differences can be seen in the tangential displacement data. Both display a small amount of initial lag, which occurs during the time frame in which most loading takes place. Load increases during the acceleration phase and typically reaches the peak prior to or coincident with a constant velocity being reached. In the thin specimens, the substrate displacement follows the bar displacement more closely after the initial lag phase, but the thick specimens show a bit more variation. This

is reasonable, because the substrate displacements are made from rigid material similar in properties to that of the bar material, while the thick specimen displacements are measured on the specimen surface, which is much more compliant.

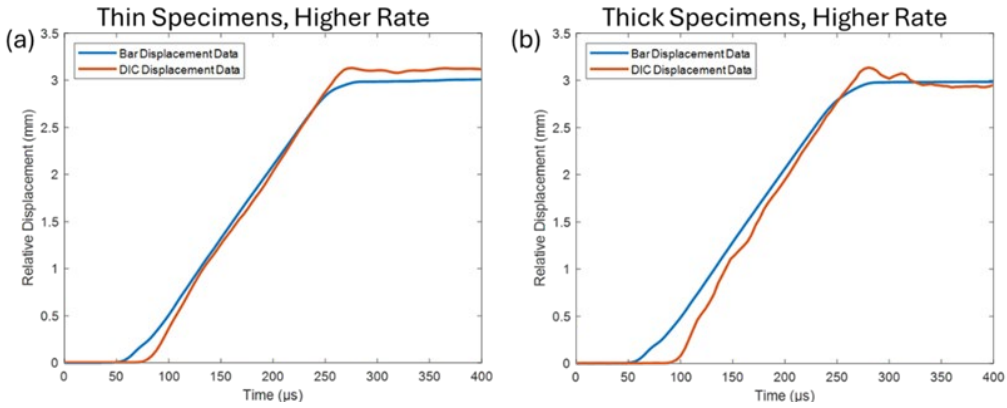

Figure 14. Bar estimate relative displacement (du_{bar}) and DIC output tangential separation comparisons for (a) thin (du_{avg}) and (b) thick specimens (du_{local}) at the higher loading rate. Both specimen designs demonstrate similar responses, but the deviation of the DIC displacement from the bar displacement response is more pronounced in the thick specimens. Responses at the lower rate are similar, just with a smaller slope and final displacement.

3.2 Identification of Timepoint at which Crack Propagation Initiates

For energy release rate calculation, traction–separation experimental data should be considered up until the timepoint at which the crack begins to propagate. Because this point is difficult to identify for Mode II characterization even under the most ideal circumstances, a load-based criteria is employed to approximate the point at which crack growth occurs. While it is possible for the crack tip to experience some yielding prior to crack growth, the point at which the load experiences the steepest decline is a likely candidate for a time in which the load-bearing capacity of the interface is reduced because of crack growth. Therefore, the time derivative of the load (Figure 15) is examined to identify the first local minimum after the peak load, and this is considered to be the point of crack initiation and the endpoint of the traction–separation behavior. Subsequent time-based plots are cropped to this endpoint, which is evaluated for each specimen.

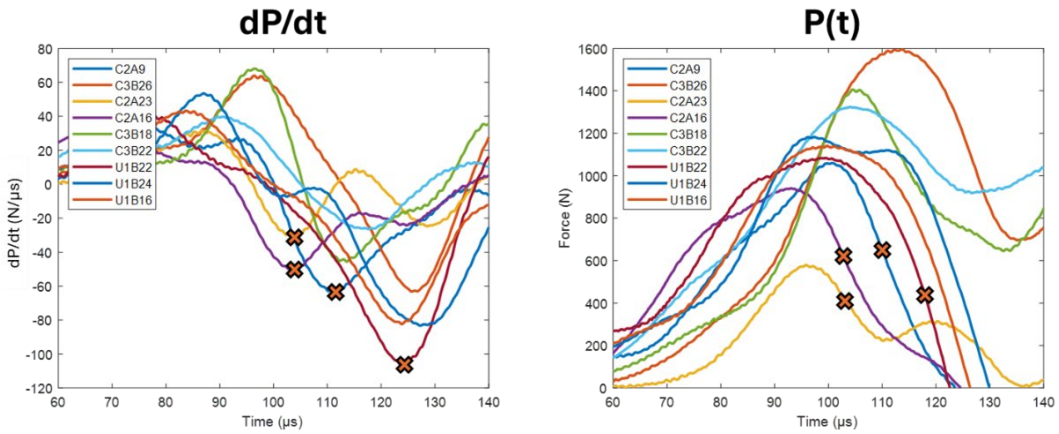

Figure 15. Representative examples showing endpoint selection based on time derivative of load (dP/dt). Example local minima are marked with corresponding points on load-time plot (P(t)). Examples are from thick specimens at the higher rate (Figure 13d), but the procedure was also used for the thin specimens.

3.3 Tangential Separation

Time series data of the tangential separation as measured using DIC analysis (du_{avg} for thin specimens and du_{local} for thick specimens, Equations 4 and 5) for each experimental group is presented in Figure 16. Data is cut off at the time of crack initiation as determined by the time derivative of the load. The spread in responses is most notable for thick specimens at the lower rate, though some variability is also visible in the thick specimens at the higher rate. Because the displacements for the thin specimens were obtained from the rigid substrates, more consistent displacement behavior is reasonable. For both specimen types, final displacements are consistently higher, which is reflected in the final computed energy release rates.

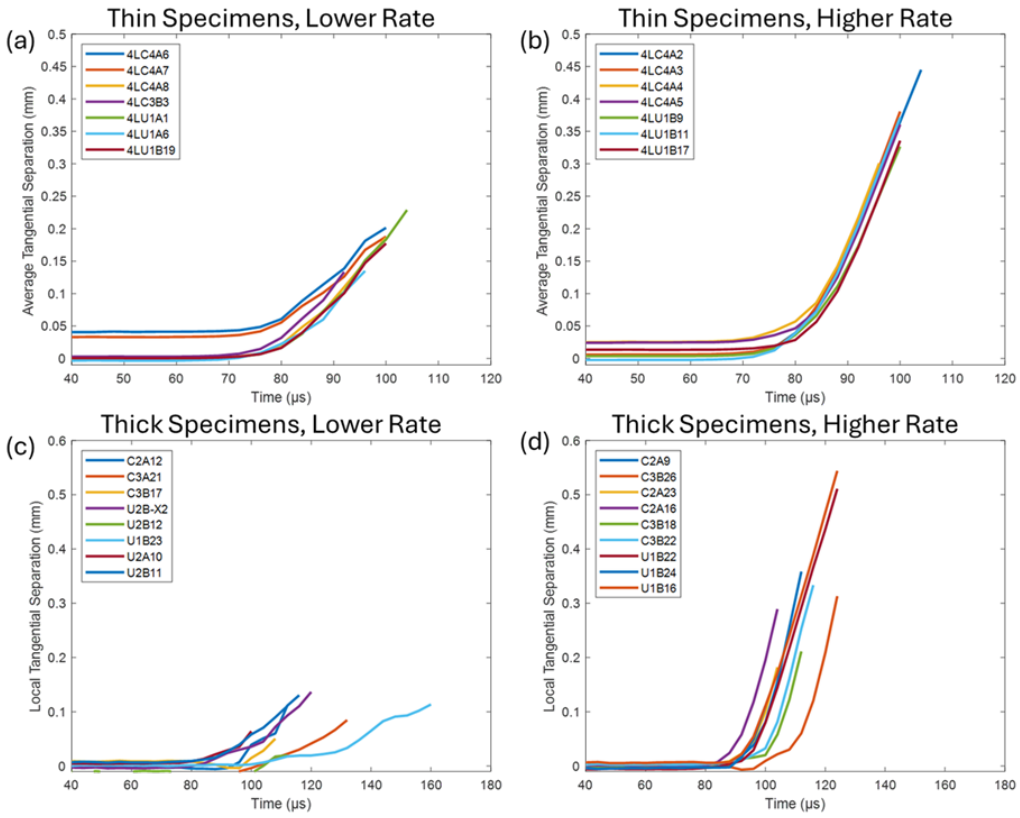

Figure 16. (a) Average tangential separation (du_{avg}, Equation 4) for thin specimens at the lower rate and (b) thin specimens at the higher rate. (c) Local tangential separation (du_{local}, Equation 5) for thick specimens at the lower rate, and (d) thick specimens at the higher rate. Variation in tangential separations is lower for thin specimens, but this is expected because those are derived from rigid substrate displacements rather than local material deformation as in the thick specimens (see Section 2.5 regarding calculation of average tangential separation).

3.4 Crack Tip Velocity

Crack tip velocities (V_{CT}, Equation 6) are presented for all experimental groups in Figure 17. Trends are largely in line with displacement data. Comparing velocity data with load data, the velocity is not constant through a significant portion of the initial loading. Thus, velocity estimates are averaged across the entire experiment, starting from the time of initial load pickup to crack initiation. In terms of the bar velocity measured after the initial acceleration phase, the lower rate corresponds to a bar velocity of approximately 5 m/s, and the higher rate corresponds to a bar velocity of approximately 15 m/s. However, in terms of the crack tip velocities, the lower rate presents with an average velocity of 3.7 m/s for thin specimens and 2.8 m/s for thick specimens (3.2 m/s combined). The higher rate presents with an average crack tip velocity of 8.8 m/s for thin specimens and 5.7 m/s for thick

specimens (7.1 m/s combined), a 105%–138% increase with a 200% increase in input pressure.

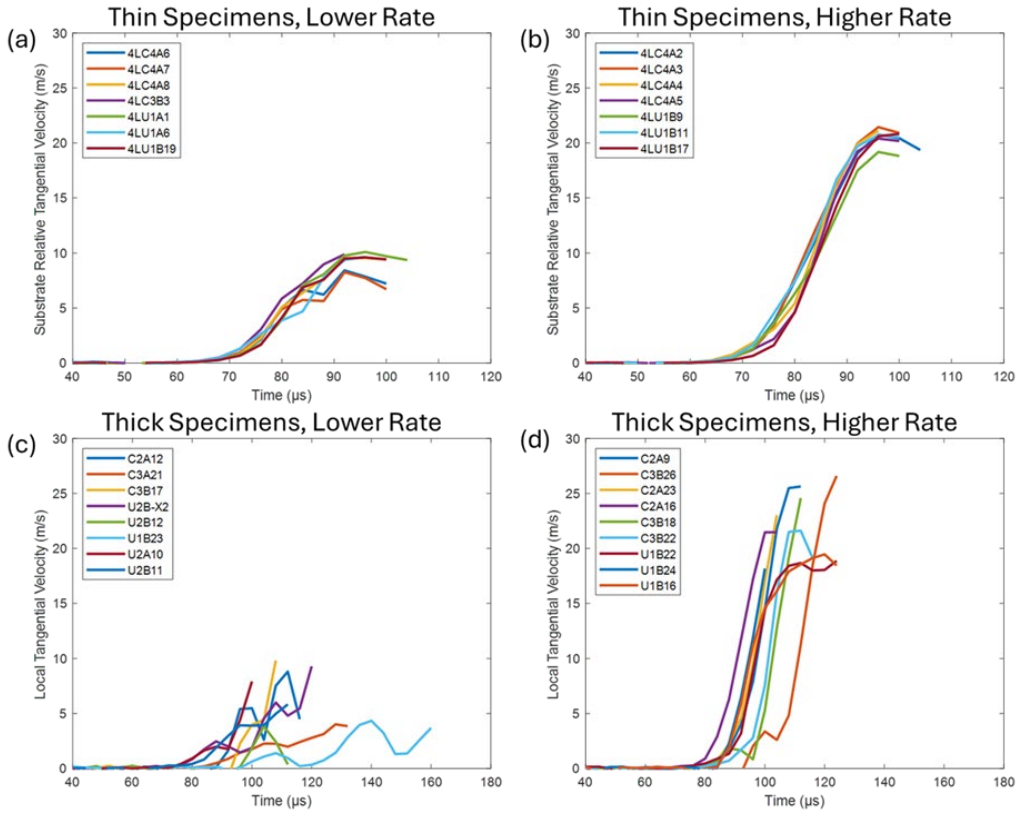

Figure 17. Approximate crack tip velocity V_{CT} for (a) thin specimens at the lower rate, (b) thin specimens at the higher rate, (c) thick specimens at the lower rate, and (d) thick specimens at the higher rate. Differences between specimen types at a given rate are reasonable given the variation in displacement behavior already noted.

3.5 Crack Tip Shear Strain Rate

The evolution of the crack tip shear strain rates ($\dot{\gamma}_{xy}$, Equation 8) over time are presented in Figure 18. Trends similar to crack tip velocity V_{CT} are observed. For the thin specimens, the peak $\dot{\gamma}_{xy}$ is approximately double at the higher rate compared to the lower rate. The data spread is a bit wider in the thick specimens, and the peaks are generally much higher over the thin specimens. However, the smaller dy in calculating du_{local} for the thick specimens (Equation 5) results in generally higher transient strain rates than in the thin specimens. At the lower rate, the average strain rate across all experiments is 1.68×10^4 s^{-1} for the thin specimens and 2.55×10^4 s^{-1} for the thick specimens. At the higher rate, the average strain rate across all experiments is 4.01×10^4 s^{-1} for the thin specimens and 5.76×10^4 s^{-1} for the thick specimens. This is reasonable, given that velocities at the higher rate were approximately double those of the lower rate. Regarding implementation in a rate-

dependent material model (e.g., Mat 240 in LS-DYNA), strain rates evaluated closer to the crack plane are preferable for input parameter determination, so the thick specimen strain rates, which are based on the actual material deformation, should take precedence over thin specimen strain rates. Because thin specimen strain rates are evaluated between the rigid substrates outside of the material, these values do confirm the general range of the strain rates but should slightly underpredict the actual value, which is consistent with the presented data.

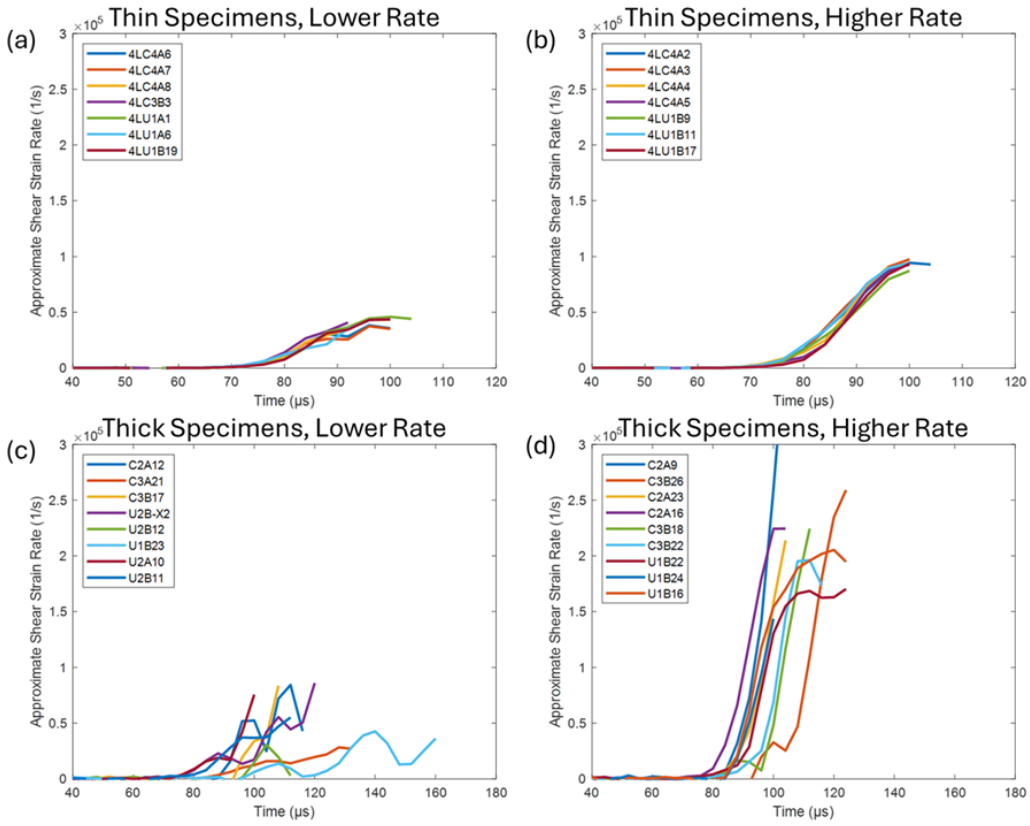

Figure 18. Approximate crack tip shear strain rate $\dot{\gamma}_{xy}$ for (a) thin specimens at the lower rate, (b) thin specimens at the higher rate, (c) thick specimens at the lower rate, and (d) thick specimens at the higher rate. Velocities are marginally higher for the thin specimens, but the evaluation distance *dy* is smaller for thick specimens (Section 2.5), increasing the apparent strain rate.

3.6 Mode II Traction–Separation Curves

Apparent traction–separation data for each experimental group is presented in Figure 19. Traction is taken to be force (Figure 13) divided by interfacial area, defined as the specimen width (z-dimension in Figure 2) multiplied by uncracked ligament length (x-dimension). Data is cropped at the point of maximum load drop, which is considered to be the failure point (example in Figure 15). Some variation in the overall shape of the curve is observed within groups, but key features are

always identifiable. Peak traction is perceived as the approximate shear strength of the material, and an initially high slope is observed and recorded. A ductile postpeak behavior is often observable, especially at the higher rate that is notably different from the experimental QS traction–separation curve, which demonstrates a sudden failure shortly after reaching peak traction. At the higher rates, peak tractions are significantly higher, and displacements before failure are much larger as well. The area under each curve is considered an approximation for G_{IIC}, and because of these clear differences based on rate, the apparent G_{IIC} increases by around 300% with the increasing rate. At the lower rate, the thin specimens have an average peak traction of 7.26 MPa, initial apparent stiffness of 887 MPa/mm, and G_{IIC} of 1018 J/m^2; thick specimens have an average peak traction of 7.86 MPa, initial apparent stiffness of 846 MPa/mm, and G_{IIC} of 671 J/m^2. Both groups combined have an average peak traction of 7.58 MPa (122% higher than QS), apparent interfacial stiffness of 865 MPa/mm (72% higher than QS), and G_{IIC} of 833 J/m^2 (1172% higher than QS). At the higher rate, the thin specimens have an average peak traction of 15.1 MPa, initial apparent stiffness of 1005 MPa/mm, and G_{IIC} of 3997 J/m^2; thick specimens have an average peak traction of 14.1 MPa, initial stiffness of 1458 MPa/mm, and G_{IIC} of 3846 J/m^2. Both groups combined have an average peak traction of 14.5 MPa (325% higher than QS), initial stiffness of 1260 MPa/mm (151% higher than QS), and G_{IIC} of 3912 J/m^2 (5873% higher than QS).

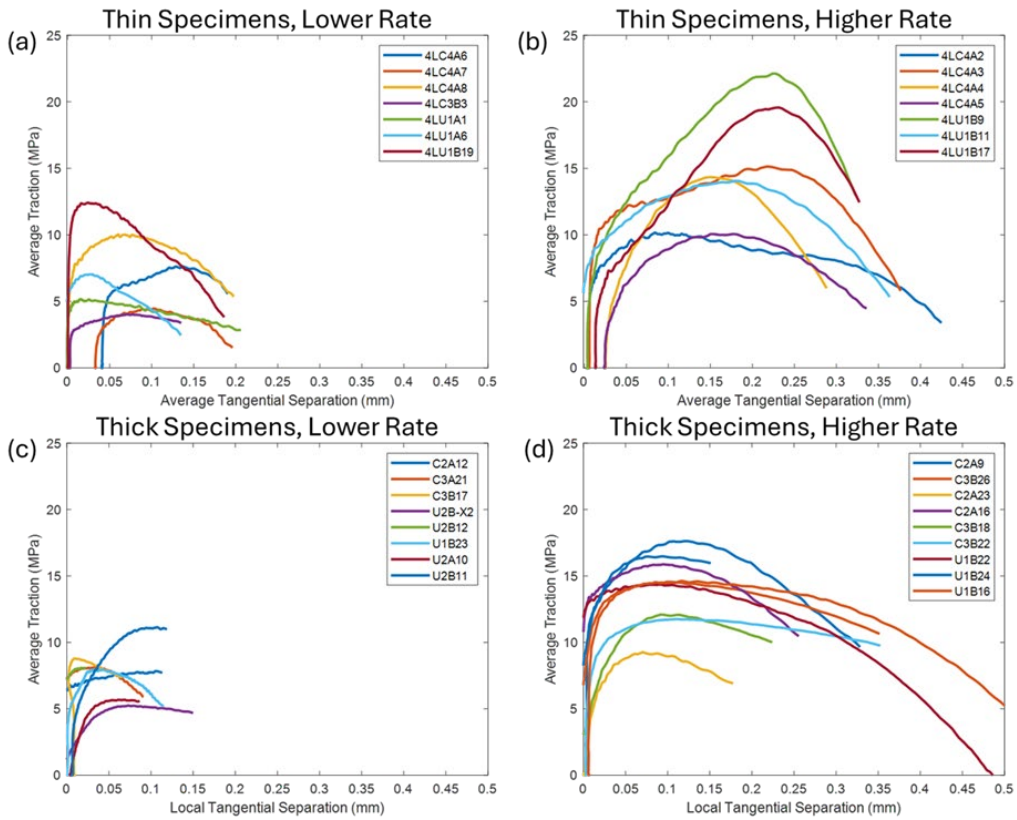

Figure 19. Experimental traction–separation data for (a) thin specimens at the lower rate, (b) thin specimens at the higher rate, (c) thick specimens at the lower rate, and (d) thick specimens at the higher rate. Maximum traction and separation both increase with increasing rate, resulting in significant increases in computed energy release rates from the lower to the higher rate for both specimen types.

3.7 Through-Thickness Shear Modulus

Another material parameter that can be estimated from the thick specimens and is informative for the analysis is the elastic shear modulus (G_{12} in the DIC coordinate system). On the thick specimens, shear strains should be (and generally are) relatively constant at moderate distances from the crack tip. By dividing the load by the total specimen area (specimen width times specimen length, z- and x-dimensions in Figure 2), far-field shear stress can be approximated, and DIC can output shear strains outside the crack plane (γ_{DIC}), which can be averaged across the entire AOI to approximate the far-field shear strain (γ_{ff}). Figure 20 presents such stress–strain data, which demonstrates an initial linear region that can be used to approximately obtain G_{12}, the through-thickness shear modulus in the loading direction. At the lower rate, G_{12} is approximately 2.70 GPa, and it is 4.12 GPa at the higher rate, which is a significant increase over the corresponding QS value of 0.309 GPa (774%–1234%) as well as the value of 0.73 GPa previously obtained through ultrasonic measurement.[8]

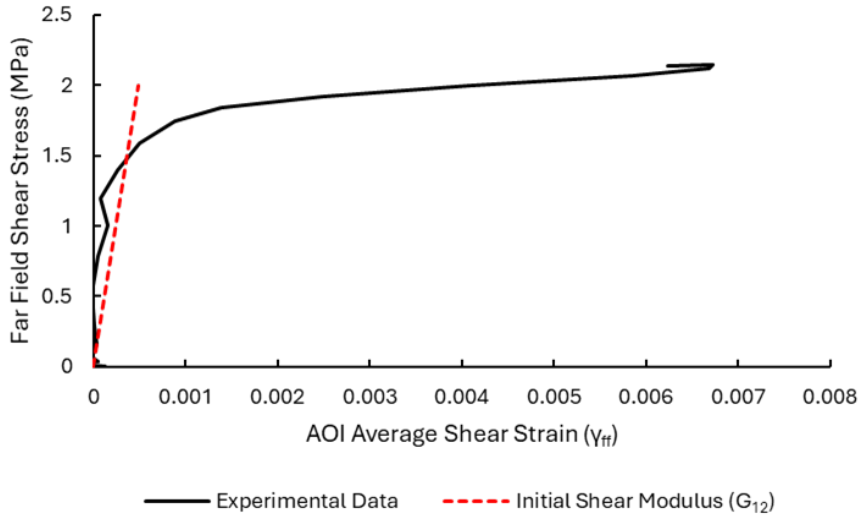

Figure 20. Example far-field shear stress–strain data with shear modulus approximation.

4. Discussion and Limitations

4.1 Applying Experimental ILS Measurements to Simulations of UHMWPE Composites

Representative experimental traction–separation data are compared with final traction–separation bilinear approximations, which can be directly input into traction–separation-based simulations as initial guesses in Figure 21. Although the overall shape is somewhat different, the trends are similar. Increases in strain rate result in significant increases in both peak shear stress and final crack tip opening displacements.

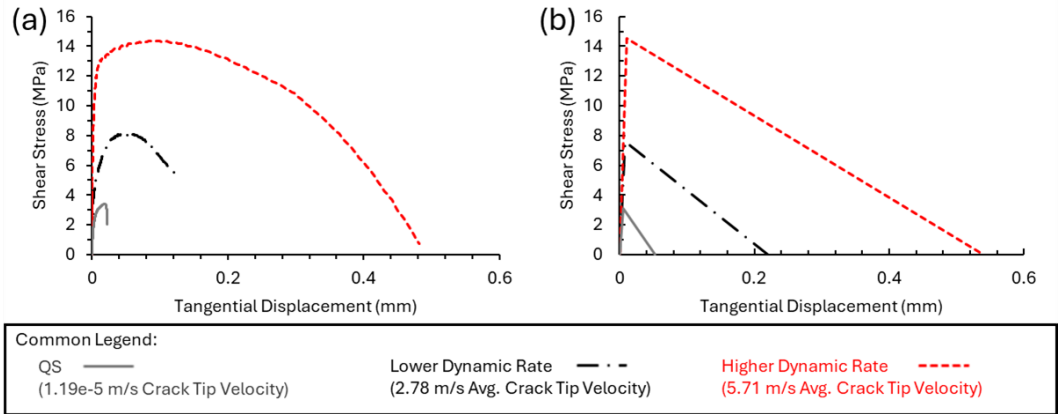

Figure 21. Comparison of (a) representative experimental traction–separation data with (b) bilinear approximations based on average parameters of τ_{max}, E_T, and GIIC as listed in the last three rows of Table 2.

From the traction–separation plots, it is clear that strain rate significantly affects the ILS response. To further examine that relationship, shear strength, energy release rate, and apparent interfacial stiffness are plotted against shear strain rate ($\dot{\gamma}_{xy}$) in Figure 22, where trends can be easily observed. Shear strength and apparent stiffness appear to increase linearly with strain rate, which is typical for UHMWPE, especially given the rate-dependent increase in through-thickness shear modulus observed in this material (Section 3.7). However, the energy release rate seems to vary quadratically with strain rate, as the increase from the lower to the higher dynamic rate is proportionally greater than the increase from QS to the lower rate. Notably, the leading coefficient appears to be relatively small (10^{-6}), so observation across a wide range of strain rates is necessary to demonstrate that this behavior is quadratic as opposed to linear. This could imply that a significant increase in energy release rate at very HSRs would be a key energy dissipation mechanism in ballistic impact scenarios.

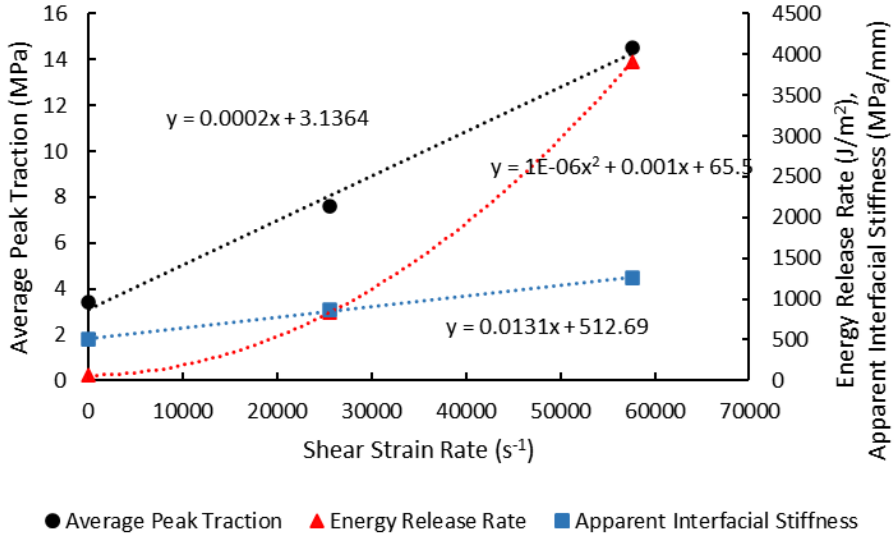

Figure 22. Average peak traction and energy release rates as a function of shear strain rate.

4.2 Limitations of Current Analysis

This study does have some clear limitations and opportunities for expansion. While confidence is good in the gross output data (e.g., loads and displacements), direct applicability of the final traction–separation data as model input may result in issues that will be further explored in future work. The most significant concern related to low confidence is because of possible nonuniformity in the stress distribution along the bond line, which requires some additional model optimization. However, if models demonstrate largely constant stresses across the entire interface, then that indicates this method is an effective means of directly extracting the Mode II traction–separation behavior of composite materials.

A significant issue in directly implementing the experimental traction–separation data is that the apparent interfacial stiffness, approximated by the initial slope of the traction–separation data, is lower than the actual interfacial stiffness because the pre-crack increases the overall specimen compliance. While a model replicating this experimental configuration should aim to match the experimental apparent stiffness, a significantly higher input stiffness corresponding more closely with the bulk shear modulus is necessary to do so. Therefore, more work must be done to accurately identify the initial stiffness as a function of increasing rate. Even so, the linear scaling of apparent stiffness with increasing shear rate suggests that a similar trend exists in the true interfacial stiffness.

Another open question that can be informed by models as well as additional experiments is the nature of the variation in energy release rate with strain rate. With the rates examined in this study, a quadratic relationship is observed. However, additional experiments at different strain rates would be helpful in confirming that this is the case, and simulations that correlate well in terms of strain rate and corresponding output data would also serve as a useful confirmation. As a long-term goal, some ballistic simulations would be necessary to identify the range of strain rates experienced during in situ loading and verify real-world applicability of these parameters.

4.3 Implications for Future Research

As noted in the results section, the velocity and strain rate are evolving over the course of each experiment, which is less than optimal but is somewhat unavoidable with the relatively weak nature of the Tensylon interface. Future experiments can investigate the use of more aggressive wave shaping techniques (very minor wave shaping was used on the higher rate experiments to produce an incident pulse similar to that of the lower rate experiments) to produce more constant velocities. However, producing approximately constant velocity at higher strain rates with aggressive wave shaping is experimentally difficult, so this will mainly be helpful in filling out the lower dynamic rates and verifying that behavior is consistent when strain rates are not changing so rapidly.

One area of investigation that is relevant but beyond the scope of this work is combined normal compression and transverse shear. It is possible that compressive stress in the through-thickness direction may change the Mode-II-type shear properties (and therefore the interfacial traction–separation behavior). Offset shear experiments can serve as a good test case and a viable means of producing in situ-type mixed mode loads, but a pure Mode II characterization procedure capable of

inducing through-thickness compression during loading as well would be a significant expansion on the experimental technique presented in this report.

5. Conclusions

A novel methodology is presented for inducing dynamic Mode II loading in soft laminated composites using tension-driven simple shear for extracting traction–separation parameters. Experiments are performed on UHMWPE Tensylon film composites using a tensile SHPB with pre-cracked (notched) specimens of 0.22- and 6.6-mm nominal thickness at a lower and a higher striker velocity inducing apparent shear strain rates of 2.55×10^4 s^{-1} and 5.76×10^4 s^{-1}, respectively, where the equivalent QS strain rate is 5.10×10^{-2} s^{-1}. Average peak traction (assuming the shear load is uniformly distributed in the uncracked ligament), apparent interfacial stiffness, energy release rate, and gross shear modulus are compared to corresponding representative data from an equivalent QS experiment. Average peak traction increases from a QS value of 3.41 to 7.58 MPa at the lower rate and 14.50 MPa at the higher rate, a 122% and 325% increase, respectively. Apparent interfacial stiffness increases from a QS value of 503 to 865 MPa/mm at the lower rate and 1260 MPa/mm at the higher rate, a 72% and 151% increase, respectively. Gross through-thickness shear modulus increases from a QS value of 0.309 to 2.70 GPa at the lower rate and 4.12 GPa at the higher rate, a 774% and 1234% increase, respectively. Approximate energy release rate increases from a QS value of 65.5 to 833 J/m^2 at the lower rate and 3912 J/m^2 at the higher rate, a 1172% and 5873% increase, respectively. While most properties demonstrate linear increases in line with previously observed behaviors, the energy release rate appears to have a mildly quadratic relationship with strain rate. This would explain how a material with relatively poor interlaminar properties under QS conditions could perform disproportionately well under ballistic impact conditions. To confirm these results, further improvements and expanded investigations, such as finite element model correlation and combined compression-shear experiments, are proposed.

6. References

1. Varun RR, Liu BG, Peerlings RHJ, Deshpande VS. Influence of microstructure on the failure of ultra-high molecular weight polyethylene composite beams impacted by blunt projectiles. Mech Mater. 2022;164:104106. https://doi.org/10.1016/j.mechmat.2021.104106

2. O'Masta MR, Crayton DH, Deshpande VS, Wadley HNG. Indentation of polyethylene laminates by a flat-bottomed cylindrical punch. Compos Part A Appl Sci Manuf. 2016;80:138–47. https://doi.org/10.1016/j.compositesa.2015.10.015

3. Cline J, Love B. The effect of in-plane shear properties on the ballistic performance of polyethylene composites. Int J Impact Eng. 2020;143:103592. https://doi.org/10.1016/j.ijimpeng.2020.103592

4. Cline J, Yeager M, Bogetti T. Determination of in-plane shear properties of UHMWPE composites for input into a thermoforming model. ASC 2019. Proc Am Soc Compos 34th Tech Conf; 2019 Aug 23–25; Atlanta, GA. https://doi.org/10.12783/asc34/31321

5. Karthikeyan K, Kazemahvazi S, Russell BP. Optimal fibre architecture of soft-matrix ballistic laminates. Int J Impact Eng. 2016;88:227–37. https://doi.org/10.1016/j.ijimpeng.2015.10.012

6. Karthikeyan K, Russell BP, Fleck NA, Wadley HNG, Deshpande VS. The effect of shear strength on the ballistic response of laminated composite plates. Eur J Mech A/Solids. 2013;42:35–53. https://doi.org/10.1016/j.euromechsol.2013.04.002

7. Gunnarsson CA, Alexander SL, Weerasooriya T. Tensile behavior of UHMWPE solid-state extrusion (SSE) film as a function of strain rate. DEVCOM Army Research Laboratory (US); 2022. Report No.: ARL-TR-9430.

8. Alexander SL, Weerasooriya T. Mechanical characterization of advanced ultra-high molecular weight polyethylene (UHMWPE) composites by ultrasonic method. DEVCOM Army Research Laboratory (US); 2021 Aug. Report No.: ARL-TR-9254.

9. Thomas FD et al. Interlaminar shear behavior of UHMWPE Tensylon® composites in quasi-static mode ii loading. ASC 2022. Proc Am Soc Compos 37th Tech Conf; 2022 Sep 19–22; Tucson, AZ. https://doi.org/10.12783/asc37/36482

10. Bensaada R, El Malki AA, Thévenet D, Arrigoni M. Interlaminar strength characterization of Tensylon® UHMWPE under multimodal loads. Procedia Struct Integr. 2023;47:503–512. https://doi.org/10.1016/j.prostr.2023.07.074

11. Boyd SE. Friction characterization of ultra-high-molecular-weight polyethylene (UHMWPE) composite materials under ambient conditions. Army Research Laboratory (US); 2018. Report No.: ARL-TR-8491.

12. Rajan S et al. Characterization of Mode I and Mode II traction–separation laws for cohesive separation of uncured thermoset tows. Int J Fract. 2020;221:25–38. https://doi.org/10.1007/s10704-019-00399-1

13. Banks-Sills L, Sherman D. Elasto-plastic analysis of a Mode II fracture specimen. Int J Fract. 1990;46:105–22. https://doi.org/10.1007/BF00041998

14. Nikbakht M, Choupani N. Fracture toughness characterization of carbon-epoxy composite using arcan specimen. Int J Aerosp Mech Eng. 2008;41:247–253.

Appendix. Digital Image Correlation Procedures for Tangential Shear Separation Quantification

A.1 Overview

For high loading rate experiments, high-speed imaging systems such as the Shimadzu HPV-2 capture images at sufficiently high rates to perform basic DIC on dynamically loaded specimens. However, the resolution of these cameras is extremely limited (312 × 260 or 0.08 MPs in the case of the HPV-2) compared to cameras used for quasi-static (QS) imaging, which offer a wide variety of higher resolutions depending on the requirements of a given experiment. For homogeneous materials undergoing simple deformation such as tension or compression, typical digital image correlation (DIC) best practices work well even at high rates and correspondingly low resolutions. However, the interlaminar shear characterization presented in this report results in highly localized deformation that pushes the capability limits of subset-based DIC algorithms in packages such as VIC-2D. This appendix discusses a few changes to typical DIC data reduction procedures, which have been adopted to enable maximal data extraction with sufficient confidence in the data integrity.

A.2 Key Terms and Concepts

In subset-based DIC algorithms, such as those in the VIC-2D program used in this study, data output is controlled by two key parameters: the subset size and the step size. A single displacement data point is calculated at the center of a square region. This square region is known as the subset. The area of the square, measured in square pixels, is referred to as the subset size. After determining the displacement of a point at the center of a given subset, the algorithm calculates the next output data point by moving the subset by a number of pixels called the step size. Care must be taken when selecting the step size. If the step size is too small and adjacent subsets are not sufficiently distinct, the displacements for multiple subsets may erroneously appear to be too similar, resulting in the introduction of bias.

A.3 Methods Used in This Study

For accurate subset-based DIC displacement and strain measurements, subsets must be uniquely identifiable by the algorithm based on variations between dark and light pixels, even when the subset has undergone substantial deformation. To ensure that this is the case, even with an optimal speckle size (3–5 pixels) and distribution (random with approximately 50% speckle coverage), it is recommended that a subset should contain at least three unique features that are 3 pixels across and separated by 3 pixels, resulting in a minimum subset size of 15 × 15 pixels^2, with

21 × 21 pixels^2 being a safer recommendation.[1] However, for low-resolution imaging experiments with nonuniform deformation, such a subset size can be overly large relative to the specimen, resulting in limited spatial resolution and over-smoothing of the deformation. For example, in this high loading rate study where the magnification of the high-speed imaging systems is typically 0.08 mm/pixel, the subset size would correspond to a 1.68 × 1.68 mm^2 area at the safe 21-pixel subset size. This subset size would be undesirably large since the specimen is only 6.6 mm in the through-thickness direction. Specifically, to get sufficient data for the small specimens in this study using such a subset size, the subsets would have to be overlapped by a considerable percentage of the subset area, which can lead to bias (Section A.2). Therefore, VIC-2D allows subset sizes as small as 9 × 9 pixels^2, though a trial-and-error process is necessary to ensure that sufficient correlation is maintained, and measurement error is minimized. For this study, consistent results were achievable across all experiments with a 13 × 13 pixels^2 subset size, which brings the spatial size of the subset to approximately 1 × 1 mm^2. Obtaining correlation with the smallest possible usable subset size allows for smaller step sizes to be used, thereby reducing the risk of bias that would be caused by small step size.

For conventional DIC analysis, the recommended step size to avoid bias (defined in Section A.2) ranges from one-third to one-half of the subset size, depending on the quality of the random speckle pattern and desired spatial density of data.[1] However, for low-resolution experiments where subset size is approaching the lower limit and more data is needed, the step size can be set as low as 1 pixel. In addition to improving the density of data at the interior of the area of interest (AOI), this is especially necessary when considering the boundary extrapolation feature of VIC-2D, which is sensitive to step size.

For a relatively small AOI in a low-resolution image, ensuring sufficient data at a particular boundary is obtained can be a complex problem resulting from an interplay between the subset size, step size, and AOI size. Under normal circumstances, an optimally sized AOI will produce data points at one-half the subset size around the entire border, as the algorithm only produces data at the center of a subset. For large AOIs with high-magnification, high-resolution images, a few pixels at two edges may be lost due to suboptimal parameter selection without issue, but with images such as those used in this study, loss of a few pixels severely impacts the ability to make precise measurements at the crack plane. To mitigate

[1] Jones EMC, Iadicola MA, editors. A good practices guide for digital image correlation. International Digital Image Correlation Society; 2018 Oct. https://doi.org/10.32720/idics/gpg.ed1

this issue and also allow for data much closer to the AOI boundary, VIC-2D has a "Fill Boundary" option that extrapolates an additional half subset all around the edge using the speckle pattern deformation. Figure A-1 presents a visual comparison of the data availability with and without the use of this feature. It is important to note that the amount of boundary data that can be recovered through extrapolation in VIC-2D Version 7 is sensitive to subset and step size for reasons of algorithm implementation and resolution constraints. According to investigations incorporating both QS and high strain rate (HSR) DIC images used in this study, boundary fill is typically good for subset size n when step size is equal to 0.5*(n-1) or 0.25*(n-1) when the latter is an integer. While this is not a significant constraint for typical DIC scenarios, this can be problematic for dynamic experiments with low-resolution imaging. Instead, for such cases, a step size of 1 will reliably fill within 1 pixel of the user-defined AOI boundary, resulting in further reason to set step size to 1 for applications such as that of this study. This feature is particularly useful if separate AOIs are defined on either side of a known crack plane as seen in this study.

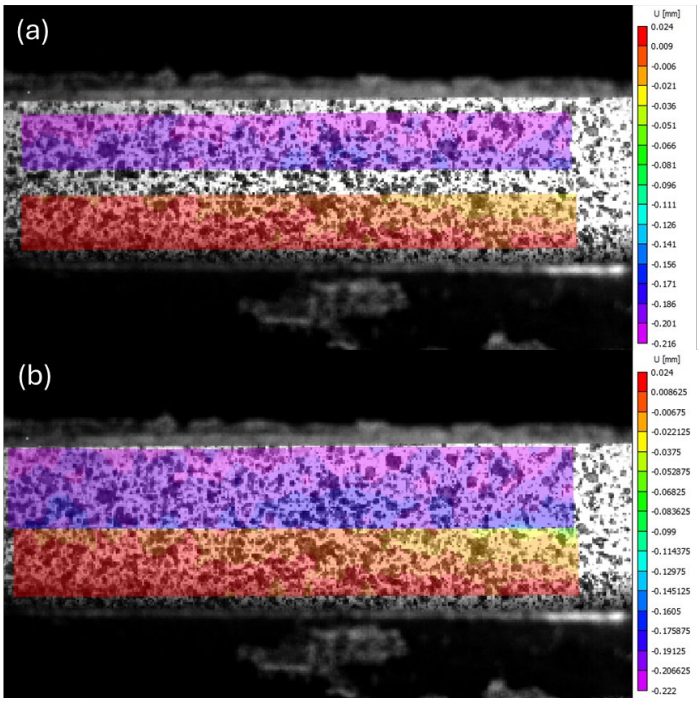

Figure A-1. Comparison of DIC output at a subset size of 13 × 13 pixels^2 and a step size of 1 pixel (a) without fill boundary and (b) with fill boundary.

For pre-cracked specimens in general, best practices dictate that the pre-crack itself should be excluded from the AOI, as the DIC algorithm assumes continuity, and if this discontinuous region is included, the algorithm will attempt to find correlation and interpolate between subsets where continuity does not—and correlation should not—exist. In this study, relative displacements about the crack tip are very large

relative to the overall deformation in the specimen, occurring in a region much smaller than the smallest possible subset size. Therefore, even though the region ahead of the crack tip is technically a continuous body, it is more reasonable to treat the uncracked ligament much the same as the pre-crack, as subsets crossing the crack plane after large deformations have taken place will lose correlation at best and produce erroneous data at worst. Thus, separate AOIs are defined for the top and bottom half of the thick pre-cracked specimen with the boundary at the crack plane. Furthermore, knowing the interaction between DIC parameters, AOI selection, and fill boundary behavior of VIC-2D, the boundaries of each AOI can be optimized for the smallest possible gap between crack tip displacement data points. Because the current set of parameters will obtain data within a single pixel of the user-defined AOI boundary, if the "Merge Polygons" option in the AOI editing tools is disabled, the upper and lower boundaries can be overlapped about the crack plane. As seen in Figure A-2, the opacity will be increased by the overlapping polygons if this is done properly. When correlation is run with this configuration, the output DIC data from each AOI will be available at adjacent pixels with no actual overlap in the data. Some iteration on positioning may be necessary to ensure that data boundaries actually correspond to the final broken halves of the specimen, but once the proper AOI definitions are obtained, this configuration will result in the best spatial resolution possible for this and similar experimental methodologies.

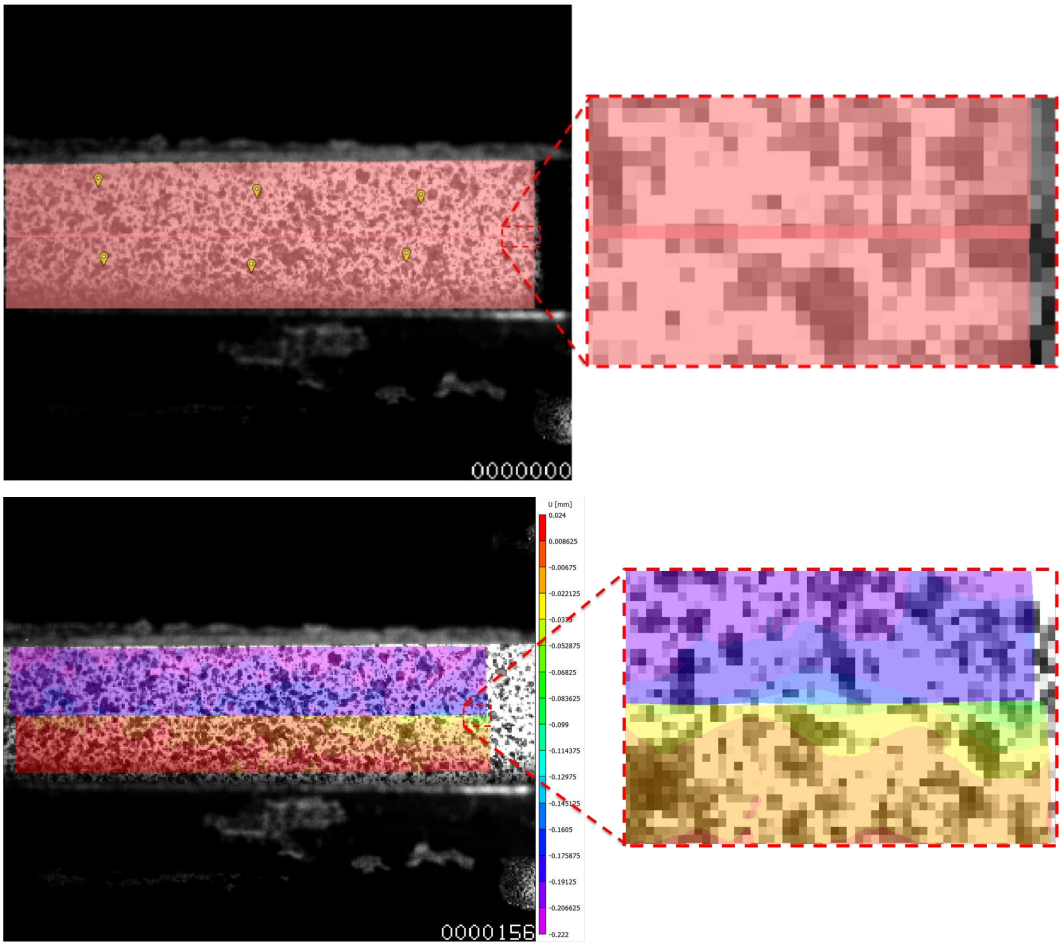

Figure A-2. Example of overlapping AOIs with corresponding DIC output.

List of Symbols, Abbreviations, and Acronyms

2D	two-dimensional
AOI	area of interest
DIC	digital image correlation
ENF	end-notched flexure
FEP	fluorinated ethylene propylene
fps	frames per second
HSR	high strain rate
ILS	interlaminar shear
NA	not applicable
QS	quasi-static
SHPB	split-Hopkinson pressure bar
UD	unidirectional
UHMWPE	ultra-high-molecular-weight polyethylene
UHS	ultra high speed

1 (PDF)	DEFENSE TECHNICAL INFORMATION CTR DTIC OCA
1 (PDF)	DEVCOM ARL FCDD RLB CI TECH LIB